

# Influence of strain rate and temperature on the mechanical behaviour of additively manufactured AlSi10Mg alloy – experiment and the phenomenological constitutive modelling

Magda STANCZAK<sup>1,2</sup>, Alexis RUSINEK<sup>2</sup>, Paula BRONISZEWSKA<sup>3</sup>,  
Teresa FRAS<sup>1</sup> and Piotr PAWLOWSKI<sup>3</sup>\*

<sup>1</sup> Department of Protection Technologies, Security & Situational Awareness, French-German Research Institute of Saint-Louis (ISL), 68301 Saint-Louis, France

<sup>2</sup> Laboratory of Microstructure Studies and Mechanics of Materials (LEM3), Lorraine University, 57070 Metz, France

<sup>3</sup> Institute of Fundamental Technological Research (IPPT PAN), Polish Academy of Sciences, 02-106 Warsaw, Poland

**Abstract.** The paper is related to the material behaviour of additively manufactured samples obtained by the direct metal laser sintering (DMLS) method from the AlSi10Mg powder. The specimens are subjected to a quasi-static and dynamic compressive loading in a wide range of strain rates and temperatures to investigate the influence of the manufacturing process conditions on the material mechanical properties. For completeness, an analysis of their deformed microstructure is also performed. The obtained results prove the complexity of the material behaviour; therefore, a phenomenological model based on the modified Johnson–Cook approach is proposed. The developed model describes the material behaviour with much better accuracy than the classical constitutive function. The resulted experimental testing and its modelling present the potential of the discussed material and the manufacturing technology.

**Key words:** AlSi10Mg aluminium alloy; additive manufacturing; DMLS method; compression; SHPB; constitutive model.

## 1. INTRODUCTION

Interest in additive manufacturing (AM) technology has increased rapidly in recent years, contributing to a growing number of relevant studies and published results. According to the SCOPUS database, in 2012, 621 articles related to this topic were published, whereas, in 2017, this number increased to 4040, reaching 8485 in 2020, [1]. This tendency shows that AM technology becomes increasingly attractive, not only for the scientific world but also for industrial applications.

Among manufacturing methods in which lasers melt the metallic powder to obtain the final geometry, direct metal laser sintering (DMLS), next to selective laser melting (SLM), is one of the most frequently applied. The DMLS may be used to sinter aluminium, titanium, nickel alloys, steel, or stainless-steel powder. It provides a reliable and repeatable part quality. In the case of AM technology, choosing the metal alloy type is as important as selecting print settings, process conditions, or post-treatment of parts. The whole fabrication process affects the properties of a final product, such as the roughness, strength, ductility, or microstructure. As the technology is relatively new, compared to casting or welding, the technical aspects of the DMLS technique

are still analysed. A large part of the conducted studies refers to selecting the optimal setting for the printing process, e.g. power and track of laser, the thickness of powder layer, speed of the sintering [2]. The discussion on the printing conditions during the manufacturing using the SLM methods for aluminium powders may be found in [3]. The papers report on different laser processing conditions and their influence on the thermal behaviour of AlSi10Mg powder during printing and the resulted microstructure. When the laser power increase, the maximum temperature gradient and the size of the melted pools also increase. The process parameters determine an energy density model correlated with pores and internal defects in the manufactured part [4]. The higher porosity was related to the insufficient energy density obtained and an increase in the non-melted grains. In addition, the deposition in a precise volumetric energy density (VED) window, which is related to the laser diameter dependence, can lead to fully dense parts [5]. Various print settings were tested in the reference [6] to find the optimal process condition. They proposed a relation between the laser power and the scanning speed to the obtained porosity. The manufactured samples were characterised by the lowest obtained porosity, below 10%, when the laser energy varied between 50 J/mm<sup>3</sup>–75 J/mm<sup>3</sup> and higher than 120 J/mm<sup>3</sup>. However, the energy density of 120 J/mm<sup>3</sup> was correlated with the additional defects, e.g. the keyholes resulting from higher vaporisation. The conclusions drawn by [7] are also confirmed by [8].

\*e-mail: ppawl@ippt.pan.pl

Manuscript submitted 2021-10-25, revised 2022-06-05, initially accepted for publication 2022-06-06, published in August 2022.

In the laser sintering methods, the authors of [9] distinguished two main types of solidification. Typically, for pure or low-alloy metals (e.g. Ti6Al5V), the microstructure may be characterised by long and columnar grains formed over the printed layers. The solidification mechanism called epitaxial growth [9] takes place along the direction of the maximum thermal gradients. It requires stable planar fronts without local perturbations in the material structure caused by an additional amount of the alloying elements. In the second case, in the structures of medium- and high alloy metals (such as the 18Ni300 maraging steel or AlSi10Mg aluminium), the grains are directed toward the centre of the melt pool. The solidification process is characterised by an expulsion of hemispherical grains forming a fine cellular structure. Different combinations of the print parameters, e.g. a scanning strategy, can strongly influence the solidification process of the melted powder. For certain powders, a unidirectional scanning can lead to the strongest texture. However, it can also generate tilts of the texture perpendicular to the scan vectors. A rotation between printed layers results in better grains and a more substantial texture for the structures manufactured from pure and low-alloy metal powders. Because anisotropy characterises the additively manufactured samples, the rotation and overlapping of layers are often applied to increase the randomness of the adjacent tracts. Thereby, this effect improves the homogenisation of the properties.

Understanding the effects of the structural anisotropy and the influence of the residual stresses on mechanical properties of the layered-built samples is another topic extensively discussed in the literature. Segebade *et al.* [10] performed tension tests of AlSi10Mg aluminium samples to define the material behaviour. The obtained results indicate that the build direction does not affect significantly hardening curves. However, it was observed that the horizontally built samples reached a slightly higher strain limit, which was attributed to the heat treatment process. This post-process facilitates relieving stresses and leads to softening of the material and improving ductility and creep resistance. Entirely different conclusions on the influence of the printed direction were drawn, see e.g. [11, 12]. The conducted research correlates the obtained results with the position of the sample on the build platform. Delcuse *et al.* [12] tested, among other effects, the effect of the build orientation on the porosity and mechanical properties of an auxetic structure made with the IN718 alloy. The studies prove that the horizontally printed auxetic structures exhibit higher yield stress, stiffness, and plastic work during the tensile test. However, Poisson's ratio is independent of the sample position during additive manufacturing.

The effect of the heat treatment is often discussed in the literature concerning AM technology. Post-processing can change the mechanical properties, like hardness and ductility, and influence the microstructure. Zyguła *et al.* [13] compared the mechanical properties and microstructure of the AlSi10Mg samples as built and after heat treatment. Then, the characteristics of the samples printed additively were confronted with the values describing samples made with a cast alloy. In both cases, the heat treatment results in a reduction of the porosity. In [14], the microstructure of samples made with the AlSi10Mg aluminium alloy as fabri-

cated and after heat treatment were discussed in detail. It was concluded that the annealing at 300°C for 2 hours caused an increase in precipitations of the fine Si phase within the columnar  $\alpha$ -Al matrix. The treatment at the temperature of 530°C for 6 hours resulted in forming a stable intermetallic phase and the microstructural equilibrium. It has been observed that each subsequent heat treatment increases the ductility and reduces the stress values obtained during tensile tests.

So far, many conducted studies, e.g. [15, 16], are related to the tensile tests, therefore, to complete the conclusions presented there, the results presented in this paper concern AlSi10Mg structures manufactured by the DLSM method subjected to compressive loading. The tested alloy is characterised by a good strength-to-weight ratio and high hardness; it also offers high corrosion resistance. Furthermore, samples printed additively from the AlSi10Mg powder have a more refined microstructure and improved strength and hardness comparing to structures produced by the conventional casting methods [6].

The tests, performed under dynamic conditions through a Split Hopkinson Pressure Bar (SHPB), allow the investigation of the strain rate and temperature sensitivity of the AlSi10Mg aluminium alloy. The given study is based on six different cases of additively manufactured samples, i.e. it accounted for three printing directions and the influence of the heat treatment or its lack. The microstructural analysis of the samples before and after the annealing allows us to observe discrepancies in the arrangement of the silicon and aluminium phases which affects the material behaviour. It also confirms the influence of the printing direction on the resulted structural anisotropy. The test results are used to identify a constitutive model and to calibrate the material parameters. The modified Johnson–Cook model accounting for the phenomenological observations is identified and validated in the experimental loading cases. The provided discussion on the microstructure and mechanical behaviour of the tested structures can be useful for designing and manufacturing the components from the AlSi10Mg aluminium powder.

## 2. SAMPLES FOR TESTING – MANUFACTURING METHOD, GEOMETRY, MICROSTRUCTURE

The samples for the material testing are manufactured by an EOSINT M 280 3D printer taking advantage of the direct metal laser sintering method [17]. During printing in the argon atmosphere, the laser beam melts subsequent powder layers. The bidirectional scanning at an angle of 67° forms a so-called "basket weave" pattern of the melt pools, which can be seen on the top surface of the printed component [18]. During the solidification process, the printing technique results in forming a fine microstructure. It also contributes to the unified macro properties of the final part. As shown in Table 1, the processing parameters have been selected to obtain the laser energy density of 50 J·mm<sup>-3</sup> (based on (1)), allowing almost solid components and neglecting the negative influence of the porosity

$$E_{\text{density}} = \frac{P_{\text{Laser}}}{v_{\text{scan}} \cdot h_s \cdot t_{\text{Layer}}} \quad (1)$$

**Table 1**  
Set of the printing parameters

Parameter of the printing process	Symbol	Value
Power of the laser source	$P_{\text{Laser}}$	370 W
Scan velocity	$v_{\text{scan}}$	1300 mm·s <sup>-1</sup>
Hatch distance of the laser scan tracks	$h_s$	190 μm
The thickness of the powder layers to be scanned	$t_{\text{Layer}}$	30 μm
Energy density	$E_{\text{density}}$	50 J·mm <sup>-3</sup>

**2.1. Description of the quasi-static and dynamic tests**

The manufactured samples are subjected to a compression loading under quasi-static and dynamic conditions. The quasi-static compression tests are performed using cylinders with the dimensions of  $\phi = 6$  mm and  $h = 9$  mm. In the dynamic compression tests performed using the Split-Hopkinson pressure bars, the cylindrical samples of  $\phi = 5.8$  mm and  $h = 3$  mm are tested. The proportion of the samples used for compression was chosen based on the work of [19]. Additionally, according to the standard ASTM D 4543, the ratio  $L/D < 2$  of the cylindrical sample should ensure that the compression process is unaffected by buckling or shearing effects. Indeed, during the performed experiments it was so – the observed compression proceeded with a homogeneous deformation. It was also a result of the application of a high-pressure grease with molybdenum disulphide ISO140, which minimized the friction effect.

To verify the effects of material anisotropy, the specimens for mechanical tests were printed along with three directions – a horizontal print [0°], vertical [90°], and at the angle of 45° to the build platform [45°], Fig. 1a. This approach follows the assumption of transversal isotropy of the printed material.

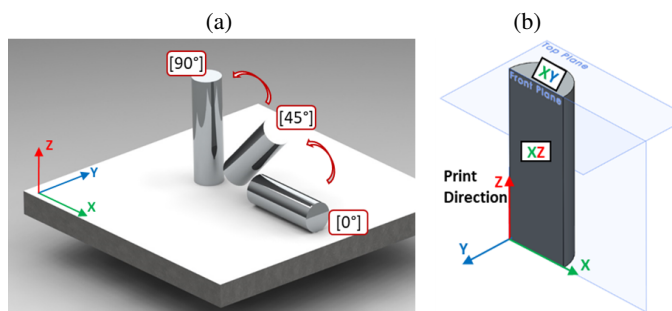


**Fig. 1.** The printing directions for the mechanical testing scheme: (a) orientation of the samples versus the build platform; (b) the observed sample surfaces for the microstructural analysis

The printed samples were lathed and subsequently cut by electrical discharge machining (EDM) to the required dimensions. The study concerns the samples as fabricated and after heat treatment, due to which internal stresses are relieved. The heat treatment is realised for 120 minutes at 300°C, following indications of the powder datasheet [20]. In conclusion, the

experimental investigation is performed for six different types of samples depending on the printing direction and the heat treatment

**2.2. Microstructure analysis of the as-fabricated and heat-treated samples**

The microstructure was observed using Olympus DSX 510 optical microscope, which may achieve 13.5X optical zoom and 30X digital zoom. For the study, the samples were polished and adequately etched. The surfaces aligned along the building direction [XZ] and the transverse surface [XY] are schematically shown in Fig. 1b. The comparison of the microstructure is based on the specimens as-fabricated (Figs. 3a–c) and after the annealing process (Figs. 3d–f).

The formation of the optically observed melt pools (Figs. 2b, c) is presented schematically in Fig. 2a. The melt pools can be related to manufacturing and the cooling process of the melted areas [21]. Visible melt pools with distinct boundaries characterise the observed surfaces for as-fabricated (Fig. 3a) and annealed samples (Fig. 3d). As a result of differences in the cooling rate, three distinct areas are formed: a fine cellular structure, coarse cellular structure, and heat-affected zone (HAZ) (Figs. 2a, c). The first zone was created towards the melt pool centre due to a slower solidification process. The region with the coarse cellular structure is the intermediate zone between the centre and the boundaries of the melt pool. The long Si particles are formed in heat-affected zones, which contact a previously solidified melt pool. The visible bright eutectic Al/Si phase of the micrographs in Fig. 3c is precipitated during the solidification process and included in the Al matrix of melt pools. It can be observed in Fig. 3f that after the heat treatment, the Si particles become greater and more visible in the fine cellular structure. During the annealing process, the Si particles diffused from the supersaturated Al/Si matrix. As a result, the precipitated grains

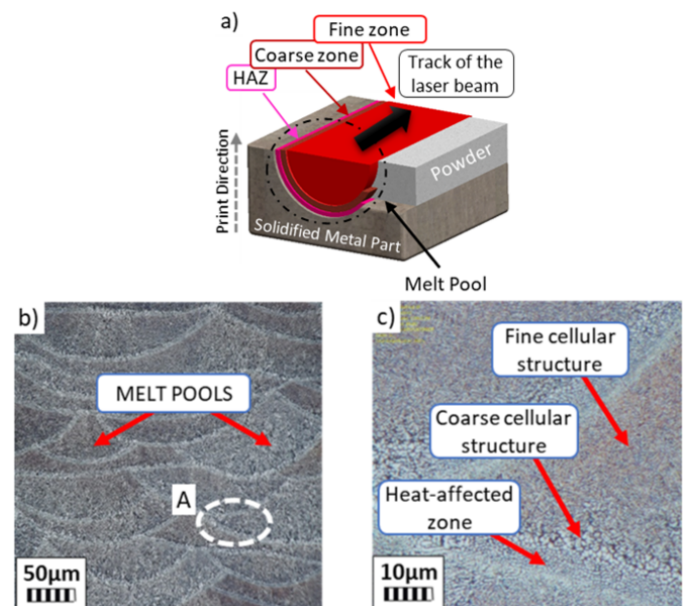


**Fig. 2.** (a) The schemes of melt pool forming and (b) the optical micrographs of the AlSi10Mg as-fabricated sample; (c) enlarged area marked 'A'

of Si are similar in shape and size to the grains in the region of the heat-affected zone (Fig. 2c). The amount and size of other particles across the aluminium matrix can strongly influence the behaviour of the manufactured samples.

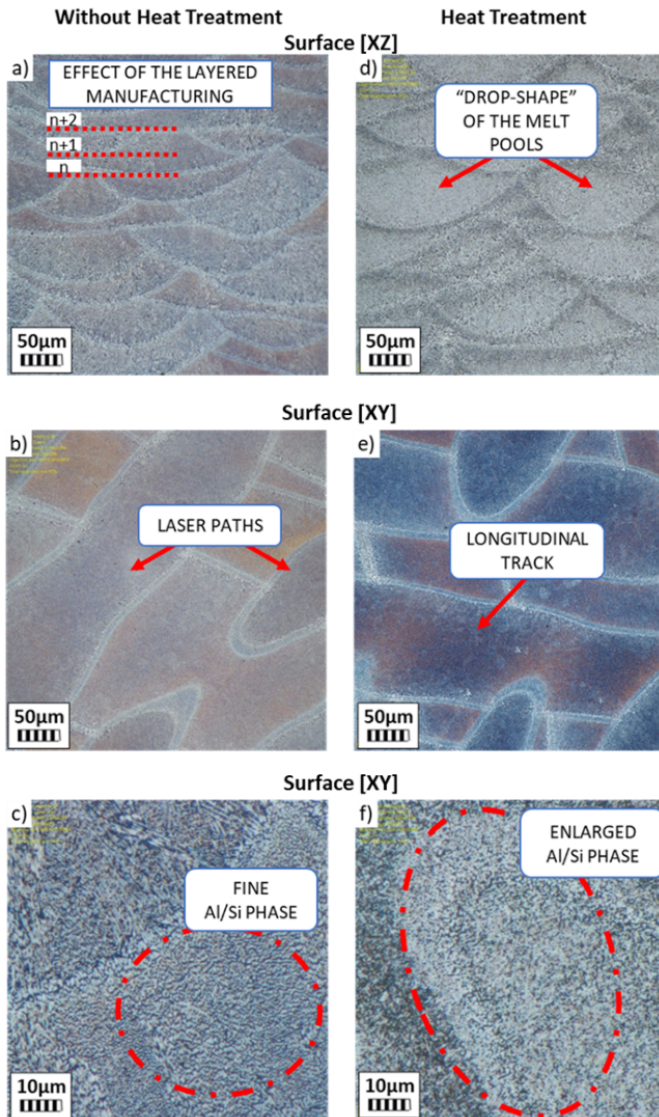


**Fig. 3.** The optical micrographs showing microstructures of the AISi10Mg samples without heat treatment (a, b, c) and annealed (d, e, f)

### 2.3. Measurement of the Vickers hardness

The hardness of the as-fabricated and annealed samples is studied with the Vickers method. The tests are performed using a Buehler's microhardness tester machine Wilson VH1202. First, an indentation mapping is performed using a 0.2 kg load with a hold time of 10 s to obtain the homogeneity along the longitudinal axes in the material. Then, to determine an average hardness value, the tests are repeated five times.

Figure 4 shows the comparison of the values obtained in the hardness tests for six types of the samples (three printing directions [0°], [45°], [90°]; heat-treated (HT) and as-fabricated (WHT)). The hardness of the HT samples decreases in com-

parison to the samples WHT. The vertically printed specimens in both conditions exhibit slightly higher HV hardness values. Moreover, the samples without heat treatment are characterised by constant hardness values, close to  $125 \pm 3$  HV. After the heat treatment, the hardness varies from  $110 \pm 4$  HV (for [45°] sample) to  $115 \pm 2$  HV (for [90°] sample).

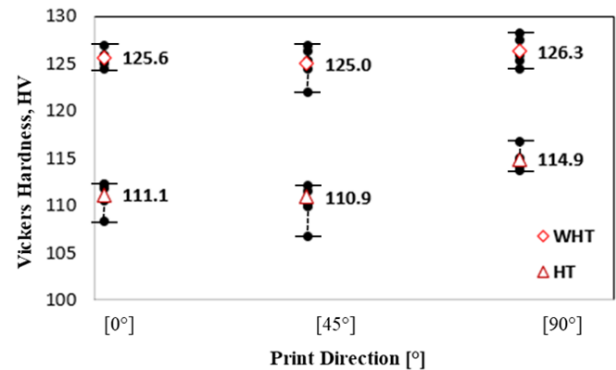


**Fig. 4.** The Vickers hardness results of the AISi10Mg aluminium alloy for the samples without the heat treatment (WHT) and after the heat treatment (HT), printed at 0°, 45°, and 90° angles to the build platform

## 3. EXPERIMENTAL TESTING OF THE MANUFACTURED SAMPLES

The samples described in Section 2 are subjected to quasi-static and dynamic compression loadings to evaluate the material properties of AISi10Mg aluminium alloy in terms of strain rate and temperature sensitivity.

### 3.1. Results of the quasi-static compression test

The quasi-static compression tests are performed using a hydraulic universal testing machine Zwick 1476 with a 100 kN load cell. The cylindrical samples with  $6 \times 9$  mm are inserted between two rigid high-strength steel blocks to avoid plastic deformation of the machine's grips. In addition, a high-pressure grease with molybdenum disulphide ISO140 [22, 23] facilitates minimising friction effects – barrelling of samples was almost not observed. Additionally, in the program WASP, used to evaluate the dynamic compression results, the correction on friction was already applied. The effect of friction on the material responses is considered negligible.

The tests are performed under three constant loading velocities at the strain rates: 0.001/s, 0.01/s, and 0.1/s. To measure the strain of the samples, the test stand is equipped with an extensometer. At the same time, the load sensor provides values of the force over time. Each test is repeated at least two times for each sample type. The details are summarised in Table 2.

The obtained true stress over true strain curves at the room temperature for different quasi-static strain rates is reported in Fig. 5. For each presented case, the influence of the printing direction is observed. The vertically printed samples [90°] are characterised by increased stress and smaller strains to fracture. The vertical samples and those printed at the angle of 45° to the build platform show a similar behaviour during the compression process, which is confirmed by the shape of the resulting true

**Table 2**

Summary of the conditions of the quasi-static compression tests

Printing direction	Strain rate	Temperature	Stress relieve
[0°] [45°] [90°]	10 <sup>-3</sup> /s 10 <sup>-2</sup> /s 10 <sup>-1</sup> /s	T <sub>room</sub>	Without heat treatment With heat treatment

stress – true strain curves. The material softening may be observed after the deformation reached the value of the true strain of 0.15 for the samples without heat treatment and 0.1 for the samples after stress-relieving.

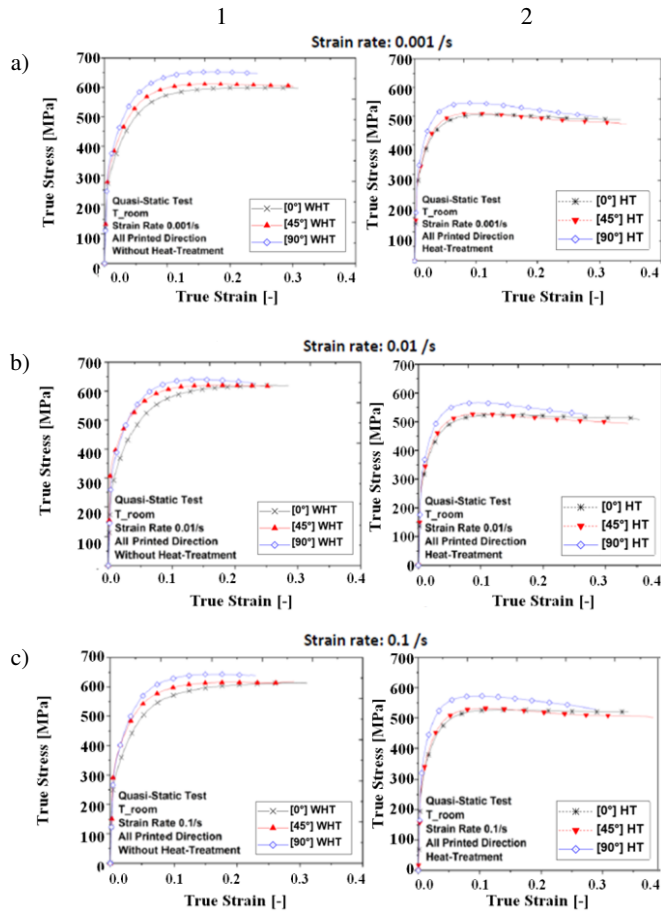


**Fig. 5.** Summary of the quasi-static compression test of the AlSi10Mg aluminium alloy given in the true stress over true strain curves

The strain rate dependency is more visible using the samples after the heat treatment. However, increasing the strain rate in the quasi-static range does not increase the stress level significantly. Therefore, the studied AlSi10Mg aluminium alloy is considered not strain rate sensitive in the quasi-static range. Comparing the results obtained for samples without heat treatment (Fig. 5(1)) and after that (Fig. 5(2)), compressed at the same strain rate, it can be observed that the annealing process causes a decrease in the obtained stress values by an average of 100 MPa and a longer deformation process. Moreover, softening in the plastic range is much more noticeable.

### 3.2. Results of the dynamic compression tests

The dynamic response of the studied material is investigated using a *Split Hopkinson pressure bar* (SHPB) test stand, presented in Fig. 6. The projectile impacts a 1.5 m long input bar, which generates an elastic incident wave  $\epsilon_I(t)$ . When the incident wave reaches the bar-specimen interface, it is split into a reflected wave  $\epsilon_R(t)$  and a transmitted wave  $\epsilon_T(t)$ . The first one goes back through the incident bar, and the second one propagates through the tested sample and then through the output bar. A full-bridge of four strain gauges and a *Vishay* conditioner are used to measure the response of the propagated waves. Further analysis is performed using the *Waves Analysis and Study Program* (WASP) based on the characteristics of the registered waves.

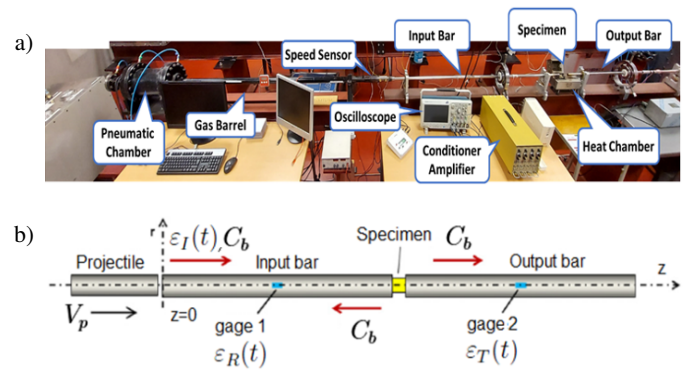


**Fig. 6.** (a) Split Hopkinson pressure bar experimental stand at the LEM 3 at the Lorraine University and (b) a schematic illustration showing its working principles [23]

The physical principles of the SHPB are based on the one-dimensional approach towards the uniaxial plane wave propagation modelling, characterised by equation (2):

$$\frac{\partial^2 U}{\partial t^2} = C_b^2 \frac{\partial^2 U}{\partial x^2} \quad (2)$$

The force equilibrium on the two end faces of the specimen is necessary to validate the performed tests. Based on Hooke's law, Ravichandran and Subhash proposed the  $R(t)$  parameter [24].  $R(t)$  should obtain a value close to zero to achieve the force equilibrium during the test. Equation (2) allows for evaluating the difference of the two acting forces ( $F_1(t)$  and  $F_2(t)$ ) on the end faces of the specimen  $\Delta F(t)$  to the average forces  $F_{avg}(t)$ . The example of the  $R$  parameter evolution, presented in Fig. 7, shows that the  $R$  parameter is almost equal to zero beyond the beginning of the performed test:

$$R(t) = \left| \frac{\Delta F(t)}{F_{avg}(t)} \right| = 2 \left| \frac{F_1(t) - F_2(t)}{F_1(t) + F_2(t)} \right|, \quad (3)$$

$$F_1(t) = E_b A_b (\epsilon_I(t) + \epsilon_R(t)), \quad (4)$$

$$F_2(t) = E_b A_b \epsilon_T(t), \quad (5)$$

where  $E_b$  and  $A_b$  are the Young modulus and a cross-sectional area of the bars.

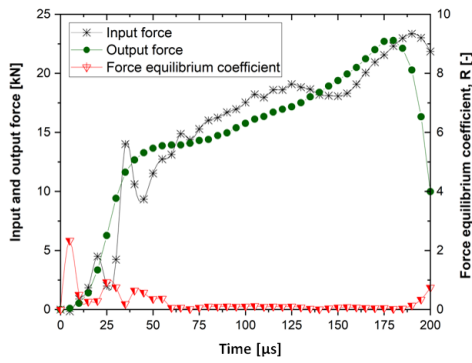


**Fig. 7.** Evolution of the force input ( $F_1$ ), output ( $F_2$ ) and force equilibrium coefficient ( $R$ ) over time

In addition, the energy balance  $W_{\text{exp}}$  (equation (6)) and the quantity of movement  $Q_{\text{exp}}$  (equation (7)) must be achieved. The obtained values for the signal of incident waves in (6) and (7) are compared with the initial energy and momentum values for the projectile equations (8) and (9):

$$W_{\text{exp}} = A_0 \rho C_b^3 \int_0^t \varepsilon_I(\xi)^2 d\xi, \quad (6)$$

$$Q_{\text{exp}} = A_0 E \int_0^t \varepsilon_I(\xi) d\xi, \quad (7)$$

$$W_P = \frac{M_P V_0^2}{2}, \quad (8)$$

$$Q_P = M_P V_0, \quad (9)$$

where  $M_P$  and  $V_0$  are mass and initial velocity of the projectile.

If the force equilibrium, energy balance, and quantity of movement are achieved, the nominal stress  $\sigma_{\text{nom}}(t)$ , the nominal strain  $\varepsilon_{\text{nom}}(t)$  and the nominal strain rate  $\dot{\varepsilon}_{\text{nom}}(t)$  can be calculated using the registered forces imposed on the samples and the resulted displacements of the bars in equations (10)–(12):

$$\sigma_{\text{nom}}(t) = \frac{E_b A_b \varepsilon_T(t)}{A_s}, \quad (10)$$

$$\varepsilon_{\text{nom}}(t) = \frac{2C_b}{L_s} \int_0^t \varepsilon_R(t) dt, \quad (11)$$

$$\dot{\varepsilon}_{\text{nom}}(t) = \frac{2C_b \varepsilon_R(t)}{L_s}, \quad (12)$$

where  $A_s$  and  $L_s$  are a cross-section and length of specimens.

The elastic wave speed  $C_b$  in a bar with the Young's modulus  $E_b$  and the density  $\rho_b$  can be described by (13):

$$C_b = \sqrt{\frac{E_b}{\rho_b}}. \quad (13)$$

The *SHPB* tests are conducted for strain rates between 1300/s and 3300/s at room temperature. The tests in each loading condition (at a specific strain rate and temperature) are repeated twice.

### 3.3. Adiabatic-isothermal correction

The performed tests confirmed that the deformation of the AlSi10Mg aluminium alloy is sensitive to temperature changes. Therefore, the adiabatic heating effect on the strains softening for the large deformation in the dynamic region is included. Knowing the temperature sensitivity  $\nu$ , the true stress under adiabatic conditions  $\sigma_{\text{Adiabatic}}$  are corrected to achieve the required isothermal results  $\sigma_{\text{Isothermal}}$ , according to (14):

$$\sigma_{\text{Isothermal}} = \sigma_{\text{Adiabatic}} + |\nu| \Delta T. \quad (14)$$

The temperature increment  $\Delta T$  during the plastic work concerning the initial temperature  $T_0$  can be estimated based on the following equations:

$$T = T_0 + \Delta T, \quad (15)$$

$$\Delta T(\varepsilon_p) \approx \frac{\beta}{\rho C_p} \int \sigma(\varepsilon_p, \dot{\varepsilon}_p, T) d\varepsilon_p, \quad (16)$$

where  $\beta$ ,  $\rho$ ,  $C_p$  are the Taylor–Quinney coefficient, the density, and the specific heat at a constant pressure of the material. The  $\beta$  coefficient corresponds to the plastic work converted into heat and depends on the strain rate of a deformation process. It is worth noticing that the estimation of this coefficient is a challenge and different methods exist to determine it correctly. In this paper,  $\beta$  is assumed as equal to 0.9, as it is usually used for metals [25, 26].

The temperature sensitivity parameter  $\nu = \partial\sigma/\partial T$  is determined based on the quasi-static tensile tests at different temperatures for horizontally printed samples. Figure 8a shows the linear curve slopes of the true stress over temperature at 6%, 8%, and 10% of deformation. The performed analysis allows determining the average temperature sensitivity parameter equal to  $\nu \approx -1.004$  MPa/K. Then, the experimental curves of the true stress at the high strain rate ranges are corrected based on (14). The example of the adiabatic-isothermal correction of the equivalent stress-equivalent strain at the different strain rates is shown in Fig. 8b.

The results in terms of material behaviour for different strain rates are reported in Fig. 9. It can be observed that in dynamic range and quasi-static regime, the AlSi10Mg aluminium alloy exhibits only a slight strain rate dependence. In addition, in the first stage of deformation (up to  $\approx 0.15$  of strain), the horizontally printed samples [0°] obtain the lowest results in terms of the stress level, then [45°] and the vertically printed [90°] are characterised as the highest obtained values. The stress values for [45°] samples without heat treatment are similar to vertical ones and, after heat treatment, closer to horizontally printed samples. The high hardening increase characterises the [45°] and [90°] samples after crossing the references strain. Moreover, it is observed that after the compression, the cross-sections for [0°] and [45°] samples are more oval than for the vertically printed samples [90°], in which cross-sections remain circular. It is an effect of anisotropy resulting from the specificity of layered manufacturing. In the case of [90°] samples, the load is applied along with the melt pools arrangement and perpendicular to the longitudinal tracks (see Fig. 3).

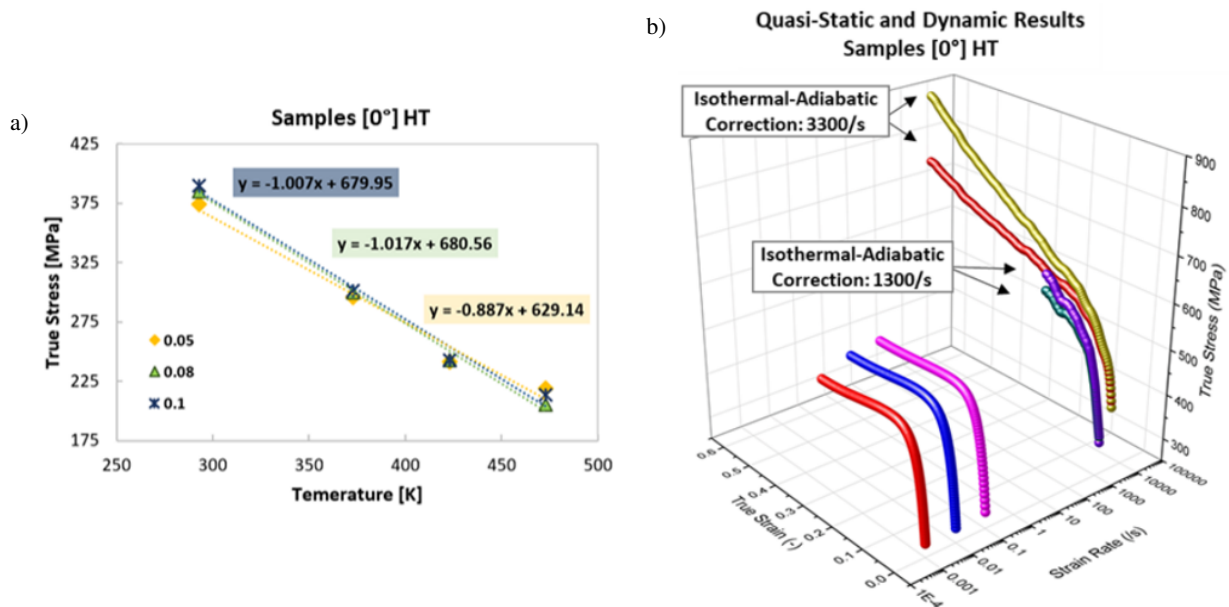


**Fig. 8.** Results for horizontally printed samples [0°] from the AISi10Mg aluminium alloy: a) temperature sensitivity of the flow stress at the 5%, 8%, and 10% strain; b) material behaviour at different strain rates under the adiabatic and isothermal conditions

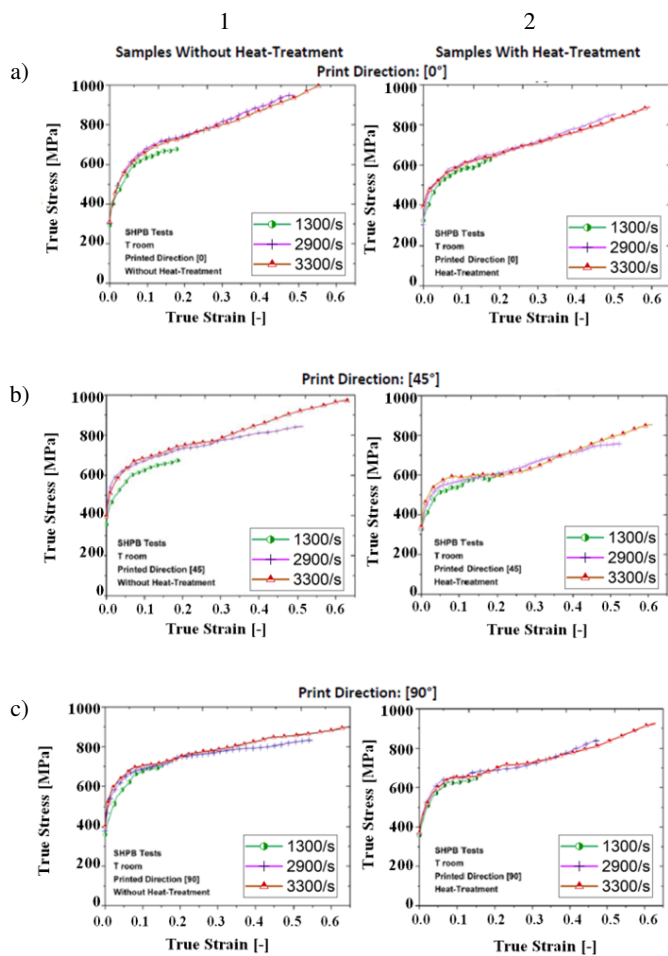


**Fig. 9.** Summary of obtained average results of true stress over true strain of a compression test on an AISi10Mg aluminium alloy sample at 1300/s–3300/s strain rates and room temperature

### 3.4. Strain-rate sensitivity of the AISi10Mg manufactured additively

The SHPB dynamic compression tests prove the slight strain rate sensitivity of the AISi10Mg aluminium alloy. The comparison of the quasi-static and dynamic results presented in the values of the true stress read for the true strain of 0.1 is presented in Fig. 10. The strain rate dependence for the tested alloy differs between the quasi-static and dynamic regions, which can be seen on the slopes of the true stress-strain rate curves (Table 3). The AISi10Mg aluminium becomes more susceptible to the strain rate in the dynamic regimes. Figures 5 and 10 show that the print direction and the performed post-processing affecting the material behaviour. Stress-relieving causes an about 80 MPa decrease in the obtained stress level. The strain rate sensitivity is more distinctly seen for the heat-treated samples in the quasi-static region (Table 3). It can be related to an arrangement of grains in

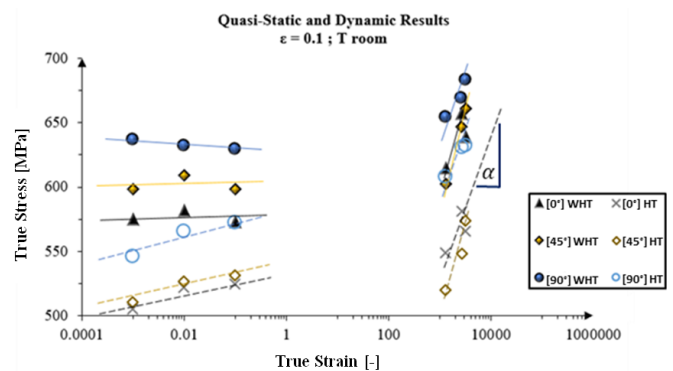


**Fig. 10.** Summary of the true stress values at 0.1 true strain for different printing directions, before heat treatment (WHT) and after stress relieving (HT)

the microstructure after the annealing process. In the dynamic regime, the heat treatment slightly affects the slope curves of the strain rate sensitivity. The highest susceptibility characterises the samples printed at the angle of 45° to the build platform to the strain rate.

**Table 3**

The slope of the true stress-strain rate curves a) at the static range; b) at the dynamic range

a) Equations of the slope curves in the static region $y = a \log(x) + b$		
Print direction	WHT	HT
[0°]	$y = -1.06x + 571$	$y = 9.67x + 534$
[45°]	$y = 0.13x + 599$	$y = 10.18x + 541$
[90°]	$y = 3.67x + 625$	$y = 13.21x + 586$

b) Equations of the slope curves in the dynamic region $y = a \log(x) + b$		
Print direction	WHT	HT
[0°]	$y = 61.7x + 422$	$y = 43.8x + 413$
[45°]	$y = 150.9x + 132$	$y = 137.4x + 92$
[90°]	$y = 73.1x + 427$	$y = 62.3x + 414$

### 3.5. Temperature sensitivity of the AlSi10Mg manufactured additively

The SHPB dynamic compression tests are performed at 100°C, 150°C, and 200°C. The constant temperature level during the test is assured by a mounted heat chamber (Fig. 6). The sensor is connected to a controller regulating the temperature in the chamber so that the sample reached the initial temperature. The compression tests are performed with an average strain rate of 2900/s.

Figure 11 presents the obtained results after adiabatic-iso-thermal correction (see Section 3.3). It is shown that with the temperature increases, the hardening stage takes place at lower stress values. However, the [0°] HT and [45°] HT samples become an exception as the obtained curves of true stress are similar for the highest temperature. This effect may be explained by a too low temperature obtained during the tests at 200°C. The highest temperature sensitivity is noticed for the horizontally printed samples [0°], whereas the lowest is registered for the samples printed at an angle of 45°. Separately for each printed direction, the values of true stress at the true strain of 0.1 are collected in Fig. 12. The graphs summarise all the results obtained from the compression tests, accounting for both strain rate and temperature influence. It is worth noticing that at dynamic rates, an increase in the temperature to 100°C causes decreasing in the stress level to those observed during quasi-static tests.

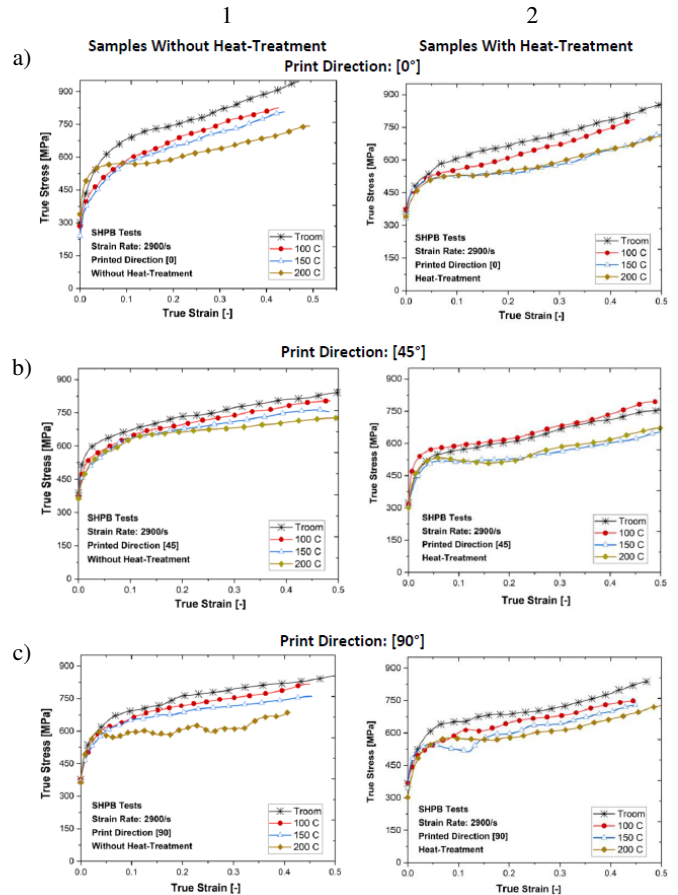


**Fig. 11.** Summary of obtained average results of true stress over true strain of dynamic compression tests at 2900/s for an AlSi10Mg aluminium alloy from 20°C–200°C

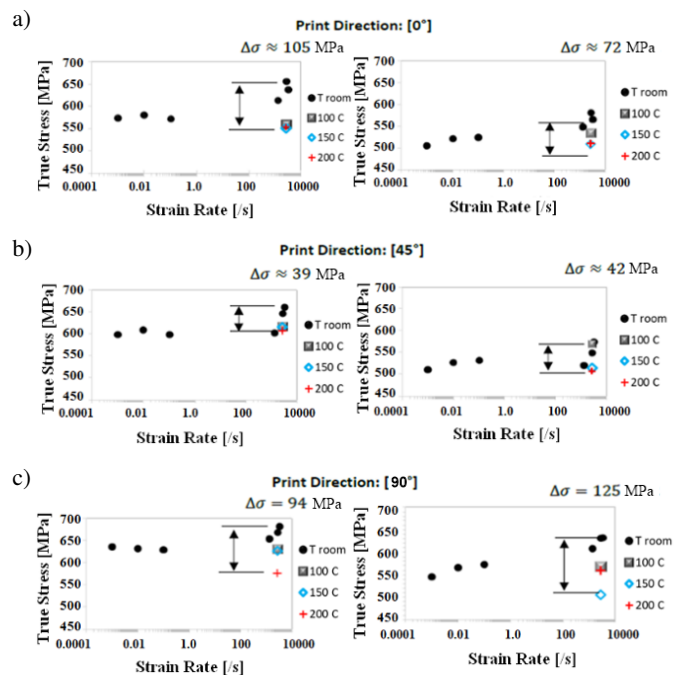


**Fig. 12.** The true stress at the true strain of 0.1 as a function of temperature and the strain rate (a–c) for different printing directions and (1–2) before and after the annealing process

#### 4. MATERIAL MODEL – IDENTIFICATION AND VALIDATION

The aim of the conducted tests is to describe the behaviour of AlSi10Mg aluminium alloy at different strain rates and temperatures. Based on these experimental observations, a proposed constitutive model of the tested material describes the flow stress in the plastic range.

Among other phenomenological models, the Johnson–Cook (JC) model is one of the most often used. The individual expressions in three brackets in equation (17) represent strain hardening, strain rate hardening, and thermal softening. It is calibrated separately using experimental data presented as stress-strain curves at different strain rates and temperatures, [27]

$$\sigma = [A + B\varepsilon_p^n] \left[ 1 + C \ln \left( \frac{\dot{\varepsilon}}{\dot{\varepsilon}_0} \right) \right] \left[ 1 - \left( \frac{T - T_0}{T_f - T_0} \right)^m \right]. \quad (17)$$

The flow stress  $\sigma$  at the strain rate  $\dot{\varepsilon}$  and at temperature  $T$  is calculated based on the equivalent plastic strain  $\varepsilon_p$  and  $A$ ,  $B$ ,  $n$ ,  $m$  are the material constants.  $\dot{\varepsilon}_0$ ,  $T_f$  and  $T_0$  are the reference strain rate, the melting temperature, and the reference temperature, respectively. The user imposed the reference values referring to the lowest strain rate and temperature values at which tests were performed. The constants above are used to approximate the thermo-visco-plastic behaviour of AlSi10Mg alloy for each direction. Additionally, the presented material parameters in Table 4 distinguish between two sets, based on the samples with and without heat treatment.

**Table 4**

The material parameters of the Johnson–Cook model for AlSi10Mg aluminium alloy developed for the samples 1) without heat treatment and 2) after heat treatment (2h at 300°C)

1) WHT	A [MPa]	B [MPa]	n [-]	C [-]	m [-]	MAPE [%]
0°	220	1184	0.437	0.0001	1.26	14.4
45°	235	1231	0.424	0.007	1.52	21.06
90°	267	1455	0.466	0.0002	1.40	23.17

2) HT	A [MPa]	B [MPa]	n [-]	C [-]	m [-]	MAPE [%]
0°	189	801	0.304	0.0009	1.33	12.92
45°	237	639	0.284	0.0001	1.34	17.56
90°	263	824	0.341	0.0018	1.31	10.49

Due to the limitations of the JC model, the constitutive model is often modified to fit the registered material behaviour or to minimise material constants, e.g. necessary in the simulation approach [28–30]. The verified parameters of the JC material modelling. Table 4 facilitates describing the AlSi10Mg material behaviour with the mean absolute percentage error (MAPE)

between 10%–23% (18):

$$\text{MAPE} = \frac{1}{N} \sum_{i=0}^N \left| \frac{\sigma_{\text{exp}} - \sigma_{\text{mod}}}{\sigma_{\text{exp}}} \right| \cdot 100\%, \quad (18)$$

where  $\sigma_{\text{exp}}$  is the experimental stress values,  $\sigma_{\text{mod}}$  is the predicted stress value, and  $N$  is the number of the fitted points.

Due to the complexity of the obtained experimental characteristics of the printed alloy, the JC model has allowed determining with good accuracy only at the first stage of the plastic work. However, the tested alloy is characterised by the softening in the second plastic range at the quasi-static condition (Fig. 5). To take this phenomenon into account, the JC constitutive model has been modified, and softening parameter  $P$  is introduced (equation (19)) to agree with experimental observation (Fig. 5).

$$f_P(\varepsilon_p) = 1 - P\varepsilon_p. \quad (19)$$

Figure 10 shows that the AlSi10Mg alloy is characterised by two ranges of strain rate sensitivity for the quasi-static and dynamic regions. However, the classic JC model does not consider a nonlinear strain rate sensitivity. Therefore, the nonlinearity of the strain rate influence is extended by the following equation:

$$f(\dot{\varepsilon}) = 1 + C_1 \ln \left( \frac{\dot{\varepsilon}}{\dot{\varepsilon}_0} \right) + C_2 \ln \left( \frac{\dot{\varepsilon}}{\dot{\varepsilon}_0} \right)^k. \quad (20)$$

As the dynamic process is related to converting the part of the plastic work into heat and cannot be dissipated along with the specimen, the isothermal-adiabatic corrections are introduced (see Section 3.3). Therefore, the softening visible in the quasi-static range is not observed in the dynamic results. However, this phenomenon is also not neglected, and the developed model allows us to distinguish the material behaviour at different strain rates. Equation (21) presents the final constitutive model for the AlSi10Mg aluminium alloy, in which the flow stress is a sum of the two ranges of the equivalent stress:  $\sigma_I$  (up to the reference strain under a visible softening) and  $\sigma_{II}$  (in which the hardening in the dynamic region occurs)

$$\sigma_f = \sigma_I + \sigma_{II} \langle \varepsilon_p - \varepsilon_{\text{ref}} \rangle^0, \quad (21)$$

where  $\varepsilon_p$  is the equivalent plastic strain and  $\varepsilon_{\text{ref}}$  is the reference strain for which the softening does not occur in the dynamic region. The Macaulay notation is defined by using equation (22)

$$\begin{cases} \langle \cdot \rangle = 0, & \cdot < 0, \\ \langle \cdot \rangle = 1, & \cdot \geq 0. \end{cases} \quad (22)$$

Then the first part of (21) can be described as the relations presented by equations (23)–(26)

$$\sigma_I = f_I(\varepsilon_p) \cdot f(\dot{\varepsilon}) \cdot f(T), \quad (23)$$

$$f_I(\varepsilon_p) = (A + B_1 \varepsilon_p^n) (1 - P\varepsilon_p), \quad (24)$$

$$f(\dot{\varepsilon}) = 1 + C_1 \ln \left( \frac{\dot{\varepsilon}}{\dot{\varepsilon}_0} \right) + C_2 \ln \left( \frac{\dot{\varepsilon}}{\dot{\varepsilon}_0} \right)^k, \quad (25)$$

**Table 5**

The material parameters of the proposed material model developed for the samples 1) without heat treatment 2) after heat treatment (2h at 300°C)

1) WHT	A [MPa]	B <sub>1</sub> [MPa]	B <sub>2</sub> [MPa]	n [-]	C <sub>1</sub> [-]	C <sub>2</sub> [-]	k [-]	m [-]	P [-]	MAPE [%]
0°	220	1184	2109	0.437	0.0001	0.0005	2.164	1.26	1.23	2.34
45°	235	1231	2505	0.424	0.007	0.0001	2.006	1.52	1.40	3.20
90°	267	1455	2854	0.466	0.0002	0.0003	2.247	1.40	1.61	2.67
2) HT	A [MPa]	B <sub>1</sub> [MPa]	B <sub>2</sub> [MPa]	n [-]	C <sub>1</sub> [-]	C <sub>2</sub> [-]	k [-]	m [-]	P [-]	MAPE [%]
0°	189	801	1728	0.304	0.0009	0.0007	1.906	1.33	1.12	2.94
45°	236	639	1594	0.284	0.0001	0.0067	1.510	1.34	1.04	2.70
90°	263	824	2209	0.341	0.0017	0.0176	0.898	1.31	1.51	3.11

$$f(T) = 1 - \left( \frac{T - T_0}{T_f - T_0} \right)^m, \quad (26)$$

where  $A, B_1, C_1, C_2, P, n, m, k$  are material constants,  $\dot{\epsilon}$  – the strain rate,  $\dot{\epsilon}_0$  – the reference strain rate,  $T_f$  – the melting temperature and  $T_0$  is the reference temperature.

After exceeding the value of the reference strain, the second part of (21) describes the equivalent flow stress as presented by (27) and (28). The material constant  $B_2$  determines the second hardening stage, visible at the dynamic conditions. The function  $\tanh(\dot{\epsilon})$  allows not to consider the effect of the material hardening in the quasi-static region

$$\sigma_{II}(\epsilon_p, \dot{\epsilon}) = f_{II}(\epsilon_p) \cdot f(\dot{\epsilon}) \cdot (\epsilon_p - \epsilon_{ref}) \cdot \tanh(\dot{\epsilon}), \quad (27)$$

$$f_{II}(\epsilon_p) = B_2 \epsilon_p. \quad (28)$$

The final equation describing the characteristics of the AlSi10Mg aluminium alloy can be presented by (29):

$$\sigma_f = f_I(\epsilon_p) \cdot f(\dot{\epsilon}) \cdot f(T) + f_{II}(\epsilon_p) \cdot f(\dot{\epsilon}) \cdot \tanh(\dot{\epsilon}) \cdot \langle \epsilon_p - \epsilon_{ref} \rangle. \quad (29)$$

The obtained material constants are presented in Table 5, which have been gathered due to comparing the forecast values with the experimental stress values using the root mean square error (RMSE) approach. Figs. 13a, b present the curves modelled using the JC model and the curves obtained after the correction due to the proposed model. The modified JC model allows for ten times lower error between the model and the experimental data (Table 6). To determine the material model parameters that characterised AlSi10Mg alloy, the observation that the aluminium exhibits different mechanical properties dependent on the post-processing must be considered. In addition, the melt pools arrangement influences the obtained stress results. Therefore, the constitutive parameters must be distinguished for each print direction. For a simplification, it is assumed that the reference strain  $\epsilon_{ref}$  is equal to 0.15 for the structures without heat treatment and 0.1 for the heat-treated structures.

Consequently, the new material model describes the material behaviour with an average error of 3% compared to the exper-

**Table 6**

Comparison of the MAPE between the JC Model and the modified JC Model based on the experimental data obtained for [0°] WHT samples

Strain Rate	0.001/s	0.01/s	0.1/s	1300/s	2900/s	3300/s
MAPE – JC Model	9.65%	11.56%	10.79%	33.28%	17.33%	10.56%
MAPE – Modified JC Model	1.62%	2.04%	1.76%	5.46%	1.79%	1.35%

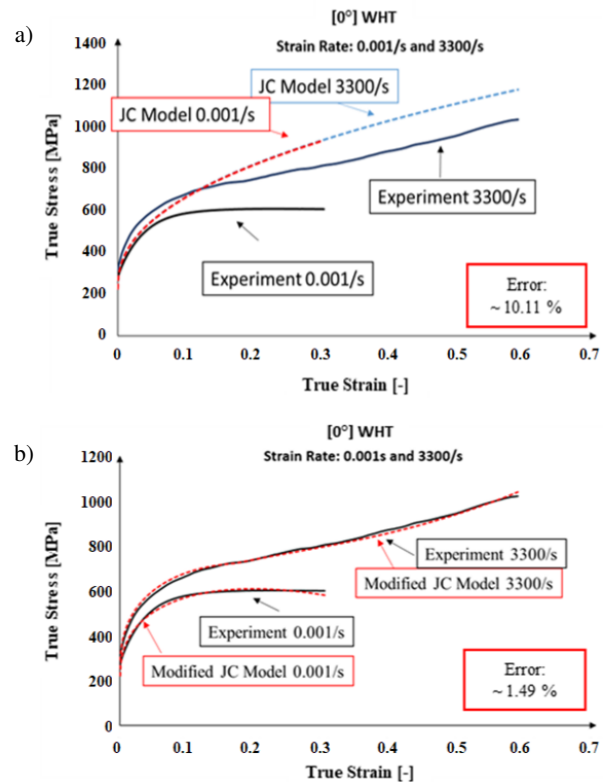


**Fig. 13.** Comparison of the experimental data for the horizontally printed samples with the curves resulted from a) JC modelling and b) modified JC modelling

perimental data (Table 5). The mean absolute percentage error is about one order of magnitude lower than that obtained based on the JC modelling. Figure 14 presents the development of the equivalent stress surfaces depending on the equivalent strain and strain rates for the horizontally printing direction.

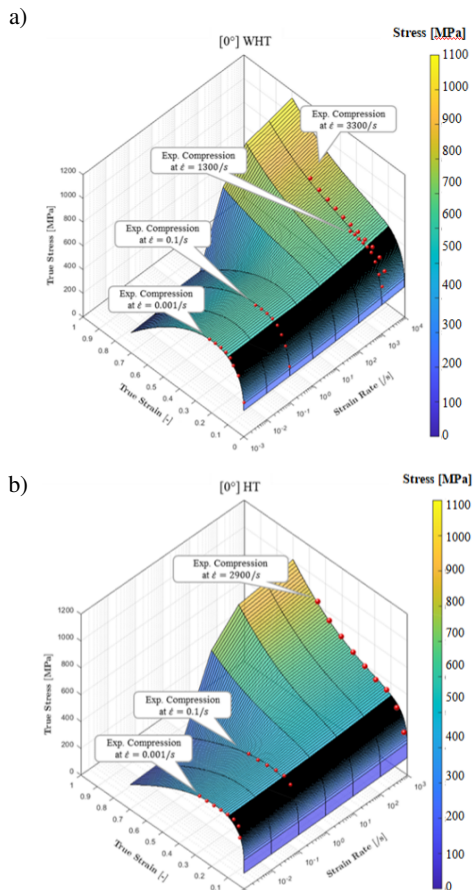


**Fig. 14.** Effects of strain rate on the equivalent stress over plastic strain at the room temperature based on the modified JC model parameters obtained for the horizontally printed samples a) without the heat treatment and b) with the heat treatment

As it is presented in Section 3, the tested AlSi10Mg aluminum manufactured additively is characterized by a certain anisotropy – in three tested print directions  $[0^\circ]$ ,  $[45^\circ]$ , and  $[90^\circ]$ , its behavior differs slightly (cf. Fig. 10). Furthermore, the discussion in Section 4 showed that conventional approach proposed by Johnson and Cook does not describe correctly the material behavior, due to which modifications of the original function were necessary.

There are several models suited particularly to describe anisotropic materials (like Hill'48 for orthotropic materials [31] or Barlat 89 [32]). Nevertheless, the choice of the JC model was based on its popularity (especially in numerical modelling) and a well-understood method of incorporating phenomenological effects, like strain rate and temperature, in the function describing the material plasticity. This model is by definition suitable for isotropic materials, which led to the identification of three sets of parameters separately for each print direction. At the moment, the proposed modified JC plasticity model was validated

only based on the discussed material. However, examples found in the literature may prove that other metallic alloys printed additively may demonstrate behavior eluding the classical model approximation, e.g. [33, 34]. In further steps, it may be a potentially interesting option to couple differences resulting from the anisotropy in one constitutive function. Further, a numerical simulation of the tested structures is a clear continuation of the initiated research program and as it is hereby discussed, conventional modeling is not sufficient to describe correctly the tested aluminum alloy, its modified version may be of use.

## 5. CONCLUSIONS

The present article analyses the mechanical behaviour of the AlSi10Mg aluminium alloy intended for components manufactured additively. The performed quasi-static and dynamic compression tests at different temperatures concern the samples printed by the DMLS method. The compression tests are conducted at the strain rate from 0.001/s to 3300/s and the temperatures up to 200°C. The experimental investigation evaluates the influence of the printed direction and the applied heat treatment on the material behaviour. Based on the obtained results, the following conclusions may be drawn:

1. The orientation of the sample to the built platform influences the stress-strain results significantly. The obtained stress during compression increases together with the slope of the printed sample to the build platform. Moreover, the annealing process (2h at 300°C) causes a significant decrease in stress level (up to 100 MPa) compared to the as-fabricated samples.
2. It is noticeable that the heat treatment causes a decrease in the obtained stress-strain results. It can be the effect of the observed changes in the microstructure after the stress relaxation due to the precipitation of the Si-phase within the Al/Si matrix. Before the annealing, the Al matrix supersaturated by Si particles contributes to a higher strength of the aluminium alloy. The Vickers hardness tests have confirmed the decreased hardness. It was verified that the as-fabricated samples are characterised by 125 HV, whereas the hardness of the samples decreased to 110 HV after the annealing process. What is more, after reaching the reference strain, the samples exhibit a change in the hardening (from softening in the quasi-static regime to a stronger hardening in the dynamic region).
3. The experimental approach to the behaviour of the AlSi10Mg aluminium under compression has proved that the material properties differ with the print direction and the chosen post-processing. These phenomena have been considered by the proposed modified JC constitutive model. Furthermore, the approach towards modelling considers the distinction between hardening and softening phenomena, two ranges of strain rate and temperature dependence. Consequently, the average error between the experiments and analytical results was minimised to an average error of 3%. However, much worse modelling results were obtained when the classical JC plasticity model was used, in which MAPE reaches about 15%.

The performed tests prove the complexity of the behaviour of the AlSi10Mg alloy manufactured additively. Based on the compression testing and its modelling, the obtained results complement a gap in the research on this alloy applied to the additive techniques. Indicating the best printing direction is a complex issue. The answer cannot be clearly stated because it may be chosen not only based on the type of load, but also on the final application of the printed component. It should be noted that a change of the print direction of the sample to the build platform resulted in an increase in the stress and stiffness of the material, but it was also observed that material ductility decreased. The presented study analyses the effects observed experimentally, providing a detailed discussion on the material performance, which can be useful for industrial applications and further optimisation of the manufactured parts.

### ACKNOWLEDGEMENTS

The authors would like to acknowledge the scientific and technical support from the Laboratory of Microstructure Studies and Mechanics of Materials (LEM3) at Lorraine University. They especially acknowledge the contributions of Richard Bernier and Patrick Moll during the material testing. This study was also supported by the Institute of Fundamental Technological Research Polish Academy of Sciences (IPPT PAN). The authors are grateful to Łukasz Cichacki and Jan Całka for their technical contribution to sample preparation.

### REFERENCES

- [1] Scopus database: [https://www.scopus.com/results/results.uri?src=s&sot=b&sdt=b&origin=searchbasic&rr=&sl=37&s=TITLE-ABS-KEY\(additive%20manufacturing\)&searchterm1=additive%20manufacturing&searchTerms=&connectors=&field1=TITLE\\_ABS\\_KEY&fields=](https://www.scopus.com/results/results.uri?src=s&sot=b&sdt=b&origin=searchbasic&rr=&sl=37&s=TITLE-ABS-KEY(additive%20manufacturing)&searchterm1=additive%20manufacturing&searchTerms=&connectors=&field1=TITLE_ABS_KEY&fields=) [Accessed 15 April 2021].
- [2] J. Kluczyński *et al.*, “Hot isostatic pressing influence on the mechanical properties of selectively laser-melted 316L steel,” *Bull. Polish. Acad. Sci. Tech. Sci.*, vol. 68, pp. 1413–1424, 2020, doi: [10.24425/bpasts.2020.135396](https://doi.org/10.24425/bpasts.2020.135396).
- [3] Y. Li and D. Gu, “Thermal behaviour during selective laser melting of commercially pure titanium powder: Numerical simulation and experimental study,” *Addit. Manuf.*, vol. 1–4, pp. 99–109, 2014.
- [4] J. Kluczyński *et al.*, “Influence of Selective Laser Melting Technological Parameters on the Mechanical Properties of Additively Manufactured Elements Using 316L Austenitic Steel,” *Materials*, vol. 13, p. 1449, 2020.
- [5] U.S. Bertoli, A.J. Wolfer, M.J. Matthews, J.-P.R. Dalplanque, and J.M. Schoenung, “On the limitations of Volumetric Energy Density as a design parameter for Selective Laser Melting,” *Mater. Des.*, vol. 113, pp. 331–340, 2017.
- [6] N. Read, W. Wang, K. Essa, and M.M. Attallah, “Selective laser melting of AlSi10Mg alloy: Process optimisation and mechanical properties development,” *Mater. Des.*, vol. 65, pp. 417–424, 2015.
- [7] E.O. Olakanmi, “Selective laser sintering/melting (SLS/SLM) of pure Al, Al–Mg, and Al–Si powders: Effect of processing conditions and powder properties,” *J. Mater. Process. Technol.*, vol. 213, no. 3, pp. 1387–1405, 2013.
- [8] J.-P. Kruth, S. Dadbakhsh, B. Vrancken, K. Kempen, J. Vleugels, and J.V. Humbeeck, “Additive Manufacturing of Metals via Selective Laser Melting Process Aspects and Material Developments,” in *Additive Manufacturing Innovations, Advances, and Applications*, T.S. Srivatsan, T.S. Sudarshan, Eds. Boca Raton: CRC Press by Taylor & Francis Group, 2016, pp. 69–99.
- [9] V.V. Krishnamurthy, “Additive Manufacturing of Rare Earth Permanent Magnets,” in: *Additive Manufacturing Innovations, Advances, and Applications*, T.S. Srivatsan, T.S. Sudarshan, Eds. Boca Raton: CRC Press by Taylor & Francis Group, 2016, pp. 413–429.
- [10] E. Segebade, M. Gerstenmeyer, S. Dietrich, F. Zanger, and V. Schulze, “Influence of anisotropy of additively manufactured AlSi10Mg parts on chip formation during orthogonal cutting,” *Proc. CIRP*, vol. 82, pp. 113–118, 2019.
- [11] L. Hitzler *et al.*, “Direction and Location Dependency of Selective Laser Melted AlSi10Mg Specimens,” *J. Mater. Process. Technol.*, vol. 243, pp. 48–61, 2017.
- [12] L. Delcuse, S. Bahi, U. Gunpath. Rusinek, P. Wood, and M.H. Miguelez, “Effect of powder bed fusion laser melting process parameters, build orientation and strut thickness on porosity, accuracy and tensile properties of an auxetic structure in IN718 alloy,” *Addit. Manuf.*, vol. 36, p. 101339, 2020.
- [13] K. Zyguta, B. Nosek, H. Pasiowicz, and N. Szysiak, “Mechanical properties and microstructure of AlSi10Mg alloy obtained by casting and SLM technique,” *World Sci.*, vol. 104, pp. 462–472, 2018.
- [14] N. Takata, H. Kodaira, K. Sekizawa, A. Suzuki, and M. Kobashi, “Change in microstructure of selectively laser melted AlSi10Mg alloy with heat treatments,” *Mater. Sci. Eng. A*, vol. 704, pp. 218–228, 2017.
- [15] NE. Uzan, R. Shneck, O. Yeheskel, and N. Frage, “High-temperature mechanical properties of AlSi10Mg specimens fabricated by additive manufacturing using selective laser melting technologies (AM-SLM),” *Addit. Manuf.*, vol. 24, pp. 257–263, 2018.
- [16] I. Rosenthal, A. Stern, and N. Frage, “Microstructure and Mechanical Properties of AlSi10Mg Parts Produced by the Laser Beam Additive Manufacturing (AM),” *Metallurg. Microstruct. Anal.*, vol. 3, pp. 448–453, 2014.
- [17] “EOS GmbH – Electro Optical Systems. Material data sheet. EOS Aluminium AlSi10Mg.” [Online] Available: <https://www.eos.info/en/industrial-3d-printing/additive-manufacturing-how-it-works/dmls-metal-3d-printing> [Accessed: Dec. 2020].
- [18] M.M. Attallah, L.N. Carter, Ch. Qoi, N. Read, and W. Wang, “Microstructural and Mechanical Properties of Metal ALM,” in: *Laser-based additive manufacturing of metal parts: modeling, optimisation, and control of mechanical properties*, L. Bian, N. Shamsaei, J. M. Usher, Eds., Boca Raton: CRC Press, Taylor & Francis, 2018, pp. 59–110.
- [19] N. Aboulkhair, M. Simonelli, L. Parry, I. Ashcroft, Ch. Tuck, and R. Hague, “3D printing of Aluminium alloys: Additive Manufacturing of Aluminium alloys using selective laser melting,” *Prog. Mater. Sci.*, vol. 106, p. 100578, 2019, doi: [10.1016/j.pmatsci.2019.100578](https://doi.org/10.1016/j.pmatsci.2019.100578).
- [20] “EOS Aluminium AlSi10Mg” [Online] Available: [https://fat.hommfg.com/wp-content/uploads/2020/11/EOS\\_Aluminium\\_AlSi10Mg\\_en.pdf](https://fat.hommfg.com/wp-content/uploads/2020/11/EOS_Aluminium_AlSi10Mg_en.pdf) [Accessed Jan. 2021].
- [21] F. Trevisan *et al.*, “On the Selective Laser Melting (SLM) of the AlSi10Mg Alloy: Process, Microstructure, and Mechanical Properties,” *Materials*, vol. 10, p. 76, 2017, doi: [10.3390/ma10010076](https://doi.org/10.3390/ma10010076).

- [22] B.R. Pęcherski, K. Nalepka, T. Frasz, and M. Nowak, "Inelastic flow and failure of metallic solids. Material effort: study across scales," in *Constitutive Relations under Impact Loadings*, vol. 552, T., Łodygowski, A. Rusinek, Eds., CISM, Springer, Vienna 2014, pp. 232–267, doi: [10.1007/978-3-7091-1768-2\\_6](https://doi.org/10.1007/978-3-7091-1768-2_6).
- [23] T. Frasz, "Modelling of plastic yield surface of materials accounting for initial anisotropy and strength differential effect on the basis of experiments and numerical simulation," Doctoral Thesis, Lorraine University, AGH University of Science and Technology, France, Poland, 2013, [Online] Available: <https://hal.univ-lorraine.fr/tel-01750617>.
- [24] G. Subhash and G. Ravichandran, "Split-Hopkinson pressure bar testing of ceramics," in: *Mechanical Testing and Evaluation*, 8th ed., H. Kuhn, D. Medlin (Eds.), ASM International, 2000, pp. 497–504.
- [25] A. Rusinek, R. Bernier, R.M. Boumbimba, M. Klosak, T. Jankowiak, and G.Z. Voyiadjis, "New devices to capture the temperature effect under dynamic compression and impact perforation of polymers, application to PMMA," *Polym. Test.*, vol. 65, pp. 1–9, 2018.
- [26] T. Frasz, Z. Nowak, P. Perzyna, and R.B. Pecherski, "Identification of the model describing viscoplastic behaviour of high strength metals," *Inverse Probl. Sci. Eng.*, vol. 19, pp. 17–30, 2011.
- [27] G.J. Johnson and W.H. Cook, "A constitutive model and data for metals subjected to large strains, high strain rates and high temperatures," in *Proceedings of the 7th International Symposium on Ballistics*, 1983, pp. 541–547
- [28] T. Frasz, I. Szachogluchowicz, and L. Sniezek, "Ti6Al4V-AA1050-AA2519 explosively-cladded plates under impact loading," *Eur. Phys. J. Spec. Top.*, vol. 227, pp. 17–27, 2018.
- [29] M. Stanczak, T. Frasz, L. Blanc, P. Pawlowski, and A. Rusinek, "Blast-Induced Compression of a Thin-Walled Aluminium Honeycomb Structure Experiment and Modeling," *Metals*, vol. 12, p. 1350, 2019.
- [30] T. Frasz, C.C. Roth, and D. Mohr, "Application of two fracture models in impact simulations," *Bull. Polish Acad. Sci. Tech. Sci.*, vol. 68, no. 2, pp. 317–325, doi: [10.24425/bpasts.2020.133120](https://doi.org/10.24425/bpasts.2020.133120).
- [31] R. Hill, "A theory of the yielding and plastic flow of anisotropic metals," in *Proc. R. Soc. London*, 1948, pp. 281–297.
- [32] F. Barlat, D.J. Lege, and J.C. Brem, "A six-component yield function for anisotropic materials," *Int. J. Plast.*, vol. 7, no. 7, pp. 693–712, 1991, doi: [10.1016/0749-6419\(91\)90052-Z](https://doi.org/10.1016/0749-6419(91)90052-Z).
- [33] L. Delcuse, S. Bahi, U. Gunputh, P. Wood, and A. Rusinek, "Constitutive Modelling of Laser Based Powder Bed Fusion Melted Inconel 718 Superalloy over a Wide Range of Strain Rates," *Advances in Manufacturing Technology XXXIV: Proceedings of the 18th International Conference on Manufacturing Research, Incorporating the 35th National Conference on Manufacturing Research*, IOS Press, 2021, vol. 15, pp. 198–203, doi: [10.3233/ATDE210036](https://doi.org/10.3233/ATDE210036).
- [34] Y. Zhao *et al.*, "A comparative study on Johnson–Cook and modified Johnson–Cook constitutive material model to predict the dynamic behavior laser additive manufacturing FeCr alloy," *J. Alloys Compd.*, vol. 723, pp. 179–187, 2017.